DOI: 10.13009/EUCASS2023-591
Aerospace Europe Conference 2023 – 10TH EUCASS – 9TH CEAS

Experimental measurements of radio signal attenuation and Faraday rotation due to electron number density in a plasma flow

Diana Luís[a,b†], Andrea Fagnani[a,c], Alan Viladegut[a], Bernd Helber[a], Adriano Camps[b,d,e] and Olivier Chazot[a]
[a]*von Karman Institute for Fluid Dynamics, Chaussée de Waterloo 72, 1640 Rhode-Saint-Genèse, Belgium*
[b]*Universitat Politècnica de Catalunya, UPC-BarcelonaTech, Barcelona 08034, Spain*
[c]*Vrije Universiteit Brussel, Pleinlaan 2, 1050 Elsene, Belgium*
[d]*Institut d'Estudis Espacials de Catalunya, Universitat Politècnica de Catalunya, Barcelona 08034, Spain*
[e]*UAE University, College of Engineering, Al Ain P.O. Box 15551, Abu Dhabi, United Arab Emirates*
diana.luis@vki.ac.be · andrea.fagnani@vki.ac.be · alan.viladegut@vki.ac.be · bernd.helber@vki.ac.be · adriano.jose.camps@upc.edu · chazot@vki.ac.be
[†]Corresponding author

Abstract

Spacecraft entering a planetary atmosphere are surrounded by a plasma layer containing high levels of ionization. The high electron number densities cause attenuation and rotation of the polarization of the emitted signal, leading to communication blackout. This work presents experimental measurements of radio signal attenuation and Faraday rotation due to an ionized plasma flow. These measurements are conducted at the VKI Plasmatron using circularly polarized directive horn lens antennas with a waveguide orthomode transducer. Clear attenuations are observed when the signal is propagating through the plasma, and Faraday rotation measurements show a good agreement with the theoretical estimation. Additionally, the jet temperature and electron number density distributions are experimentally measured with emission spectroscopy, and these results show a good agreement with numerical estimations. Overall, the signal propagation results comply with the temperature and electron density measurements.

1. Introduction

Spacecraft enter planetary atmospheres at hypersonic velocities generating shock waves ahead of the vehicle and consequent extreme aerodynamic heating. The high post-shock temperatures dissociate and ionize the atmospheric gases creating a plasma layer that surrounds the spacecraft. High ionization degrees affect the propagation of the electromagnetic waves emitted by the on-board communication antennas, causing attenuation and refraction of the radio waves. Extreme ionization levels lead, ultimately, to communications blackout. The radio communication blackout in an un-magnetized non-collisional plasma occurs when the characteristic frequency of the plasma layer around the vehicle exceeds the radio frequency used for communications. The ionization degree of the gas defines the plasma frequency, f_p [Hz], which is related to the electron number density, n_e [m^{-3}], as

$$f_p = \frac{1}{2\pi}\sqrt{\frac{q_e^2 n_e}{m_e \epsilon_0}} \approx 9\sqrt{n_e} \tag{1}$$

where q_e and m_e are, respectively, the electron charge and mass, and ϵ_0 the free space permittivity. Therefore, the electron number density is a crucial parameter to comprehend the blackout phenomena.

There are several techniques to measure electron number densities in a plasma flow, including Langmuir probes,[1–3] emission optical spectroscopy, and microwave reflectometry.[4–6] In this work focus is given on emission spectroscopy. Optical emission spectroscopy is a non intrusive technique that quantifies the electron number density based on broadening of an hydrogen line profile. In plasmas with electron number densities greater than 5×10^{19} m^{-3},[7] spatially and temporally resolved electron measurements can be done from the line shape of the Balmer β transition of atomic hydrogen at 486.1 nm. This line is suitable for this type of diagnostic due to its significant broadening, and its low sensitivity with ion dynamics effects and with electron temperature.[8] The line shape of the H_β transition is determined by Stark, van der Waals, resonance, natural, Doppler, and instrumental broadening mechanisms that result in a Voigt

DOI: 10.13009/EUCASS2023-591

profile.[7] Theoretical data sets of hydrogen line shapes using the whole atomic profile are available for direct comparison with experiments. Initially, the most accurate line shape calculation method for Stark broadening was based on the theory of line broadening developed by Vidal, Copper and Smith[9] (*VCS*). This model evaluates the ionic contribution to the line shape by using quasistatic ion approximation. However, measurements showed a discrepancy with the central region of Stark broadened lines when applying this model.[10,11] New Stark broadening theories accounting with ion dynamics effects have then been developed, including the *Model Microfield Method (MMM)* by Seidel[12] and the *Computer Simulation (CS)* method by Gigosos et al.[13,14] Laux et al.[7] derived numerical expressions for the Stark, van der Waals, resonance, Doppler, and natural half width at half maxima for the case of an air plasma with a small amount (a few percent) of hydrogen, and measured the electron number densities in atmospheric pressure air plasmas with 2% H_2 mixture in a 50 kW ICP torch operating at 4 MHz. Le Quang et al.[15] measured electron number densities using emission spectroscopy at operation conditions of 273 mbar and 120 mbar, respectively, for subsonic and supersonic plasma flows at the VKI-Plasmatron facility. The H_β line broadening was obtained using an initial air mixture seeded with a small amount of water.

From the beginning of space exploration, different methodologies for actively reducing the plasma layer effects on radio communication attenuation and blackout have been proposed and studied. During the 1960s, NASA conducted the radio attenuation measurement program[16] for development of diagnostics to characterize the reentry plasma parameters and for testing in-flight some mitigation methods. Those studies confirmed that the most feasible methods consisted of electrophilic injection and magnetic windows opening.[17] Conversely to flight experiments, several experimental campaigns have been performed. An extensive review of communication blackout testing in ground facilities has been presented by Luís et al.[18] Additionally, in that work, Luís et al. studied the signal propagation in an inductively coupled plasma wind tunnel using 23° beamwidth conical horn antennas in the Ka-band. Attenuation of the signal has been observed, ranging between 2 and 15 dB depending of the testing conditions. This attenuation increased with numerically obtained electron number densities. Preliminary evidence of Faraday rotation effects caused by the plasma have also been stated, but not quantified. Additionally, they have observed ripples on the signal due to reflections on the chamber walls.

The work presented hereafter is integrated in the Horizon 2020 MEESST (Magnetohydrodynamic Enhanced Entry System for Space Transportation) project,[19] which aims at designing and testing a proof-of-concept magnetic shielding device to mitigate radio blackout and to reduce heat flux upon the surface of the spacecraft during atmospheric entry. Analytical work[20,21] showed that the magnetic field required to allow the communication frequencies to penetrate the reentry plasma and the reduction of the heat flux must be of the order of 1 T.[22]

As part of the project, this work presents the effects of an ionized medium on the propagation of the radio signal through an air plasma flow produced with the Inductively Coupled Plasma (ICP) generator in the VKI-Plasmatron facility. The characterization of the radio wave propagation and attenuation through the plasma is conducted resorting to directive horn lens antennas aligned perpendicularly to the flow. The experimental setup also allows to estimate the Faraday rotation caused by the flow. Additionally, temperature and electron number density measurements are conducted by measuring the Stark broadening of the H_β line using high resolution emission spectroscopy. These measurements are used for comparison and correlation with the signal attenuation and rotation analysis.

2. Radio communication theory

2.1 Signal propagation in ionized mediums

The characteristics of electromagnetic wave propagation in the atmosphere depend strongly on the operating frequency. The ionosphere has a major effect on the propagation at medium and high frequencies (0.3-30 MHz), because radio waves in this frequency range are effectively reflected. For frequencies above 30 MHz, the waves propagate through the atmosphere with small attenuation, allowing satellite and deep space communications. At frequencies above 10 GHz, atmospheric conditions play a major role in the signal propagation.[23]

The ionosphere is a region of highly charged particles as an ionized gas or plasma. As such, the ionospheric propagation theory can be extended to plasma flow on ground facilities. The "reflections" from the ionosphere are produced by the actual "refraction" as the wave propagates through this region. The refraction properties of a medium are characterized by the index of refraction n, which can be estimated using the Appleton-Hartree equation[24] derived from the Maxwell's equations and the momentum conservation of electrons as

$$n^2 = 1 - \frac{\left(\frac{f_p}{f}\right)^2}{1 - \frac{i\nu}{2\pi f} - \frac{\left(\frac{f_b}{f}\right)^2 \sin^2\theta}{2\left[1-\left(\frac{f_p}{f}\right)^2 - \frac{i\nu}{2\pi f}\right]} \pm \sqrt{\frac{\left(\frac{f_b}{f}\right)^4 \sin^4\theta}{4\left[1-\left(\frac{f_p}{f}\right)^2 - \frac{i\nu}{2\pi f}\right]^2} + \left(\frac{f_b}{f}\right)^2 \cos^2\theta}} \tag{2}$$

DOI: 10.13009/EUCASS2023-591

where f is the frequency of the signal, f_p is the plasma frequency (dependent of n_e), and θ is the angle between the magnetic field vector and the wave vector. The gyroscopic frequency of electrons f_b [Hz] induced by the presence of a magnetic field B [T] is defined as

$$f_b = \frac{1}{2\pi}\frac{q_e B}{m_e}. \tag{3}$$

The electron-heavy particle collision frequency ν [Hz], for plasmas with a Maxwell-Boltzmann velocity distribution, is given by

$$\nu = \frac{q_e^4 n_e \ln(9N_D)}{64(2\pi m_e)^{1/2}\varepsilon_0^2(k_B T)^{3/2}}, \tag{4}$$

where k_B is the Boltzmann constant, T is temperature, and N_D is the Debye number given by

$$N_D = \frac{4}{3}\pi n_e \lambda_D^3 \tag{5}$$

and the Debye length λ_D [m] is

$$\lambda_D = \sqrt{\frac{\varepsilon_0 k_B T}{q_e^2 n_e}}. \tag{6}$$

In this formulation, the plasma is characterized by a complex refractive index n, consisting of a real part μ and an imaginary part χ as

$$n^2 = (\mu - i\chi)^2 = (\mu^2 - \chi^2) - i2\mu\chi, \tag{7}$$

where μ represents the effect of plasma in waves propagation bending and χ is the absorptivity responsible for attenuation effects on the travelling waves.

Figure 1 represents the variation of the refractive index with f_p/f ratio for a case of un-magnetized plasma for different ν/f ratios, and a case of non-collision plasma for different f_b/f ratios. In a non-collisional un-magnetized plasma medium (blue lines in Fig. 1), if the electron density is sufficiently high, μ goes to zero and, based on the Snell's law, a normally incident wave is reflected. This condition ($\mu = 0$) represents the cutoff frequency, from which communication blackout occurs. Otherwise, the wave penetrates the medium. Instead, in a collisional un-magnetized medium (Fig. 1a), μ is never zero and total reflection never really occurs. In this case, n^2 is complex, leading to attenuation of the signal due to the collisions. This corresponds to a wave whose amplitude is decreasing exponentially with distance, and its decay is quantified by the absorption coefficient κ [dB/m][24] as

$$\kappa = 8.69\frac{2\pi f}{c}\chi. \tag{8}$$

In the case of non-collision magnetized plasma (Fig. 1b), the refractive index is real, and the cutoff frequency is independent of θ. The presence of a magnetic field leads to a bi-refringence phenomenon, creating an extraordinary wave dependent on the strength of the imposed field, which leads to an increase of the the cutoff frequency, allowing the propagation of lower communication frequencies for the same plasma frequency. The coupling of magnetic field and collisions introduces great complications into the dispersion and absorption relationships, and it is not addressed here.

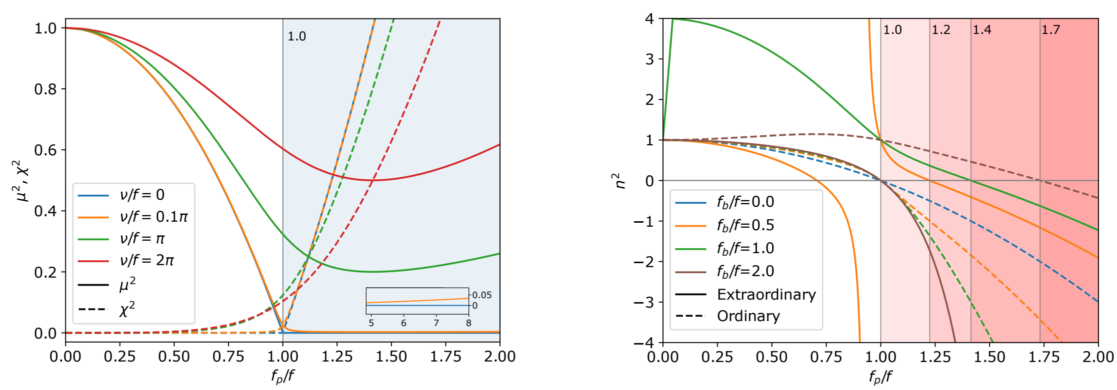

(a) Un-magnetized collisional plasma.

(b) Non-collision magnetized plasma and $\theta = 45°$.

Figure 1: Refractive index variation with plasma and signal frequencies ratio.

The total electron content (TEC) accumulated along a transmission path penetrating the ionosphere causes the rotation of the wave polarization (Faraday rotation), time delay of the signal, and a change in the apparent direction of the arriving signal due to refraction. As the rotations and time delays are non-linearly dependent on the frequency, a dispersion or group velocity distortion can also occur. The magnitude of the Faraday rotation, θ_F [rad], depends on the frequency of the radio wave f, the magnetic field strength B, and the electron density n_e [m^{-3}] of the plasma as

$$\theta_F = 2.36 \times 10^4 \frac{BN_T}{f^2}, \tag{9}$$

where N_T is the TEC [m^{-2}] expressed over a propagation path s [m] as

$$N_T = \int_S n_e(s)ds. \tag{10}$$

2.2 The scattering matrix: S-parameters

At high frequencies, a linear network is represented by its scattering matrix. This S-matrix allows to describe the properties of a multi-port network by quantifying how electromagnetic energy propagates through the network. The scattering term refers to the relationship between incident and scattered (reflected and transmitted) voltage or electric field of travelling waves. The S-matrix for a N-port network contains N^2 complex coefficients (S-parameters), each one representing the magnitude and phase of a possible input-output path. The diagonal parameters are referred to as *reflection* coefficients and the off-diagonal as *transmission* coefficients.

The waves going through the N-port are $\mathbf{a} = (a_1, a_2, ..., a_N)$ and the waves travelling away are $\mathbf{b} = (b_1, b_2, ..., b_N)$. The wave a_i going into port i is derived from the voltage wave going into a matched load. For consistency with the conversation of energy, the voltage is normalized to $\sqrt{Z_0}$, being Z_0 the characteristic impedance (often $Z_0 = 50\Omega$). The definitions of the waves a_i and b_i are

$$a_i = \frac{V^+}{\sqrt{Z_0}}, \quad b_i = \frac{V^-}{\sqrt{Z_0}}, \tag{11}$$

where V^+ is the voltage of the incident wave and V^- the voltage of the reflected wave. The relation between a_i and b_i ($i \in 1, 2, ..., N$) can be written as a system of N linear equations[25]

$$b_i = S_{ii}a_i + S_{ij}a_j, \tag{12}$$

where the j subscript stands for the port that is excited (the input port), and the i subscript for the output port. Physically, S_{ii} is the input reflection coefficient with the output of the network terminated by a matched load ($a_j = 0$); S_{ij} is the transmission from port j to port i; and S_{jj} the output reflection coefficient. The S-matrix is symmetric, which means that interchanging the input and output ports does not change the transmission properties, and therefore $S_{ij} = S_{ji}$.

3. Experimental setup and methodology

3.1 VKI Plasmatron facility

The Plasmatron at VKI is an inductively-coupled plasma (ICP) wind tunnel,[26] that creates a high enthalpy, highly dissociated subsonic gas flow for reproduction of the aerothermodynamic environment found in hypersonic flight regimes. This facility has been extensively studied by Bottin et al.[26,27] Its basic concept consists of a quartz tube surrounded by a coil, which is connected to a 1.2 MW generator that provides high voltage (2 kV) and high frequency (400 kHz) current, that induces an electromagnetic (EM) field inside the tube. The gas injection is done through an annular inlet upstream to the coil. Due to the induced EM field, the gas ionizes and the flow exits the torch to enter into a vacuum chamber of 1.4 m in diameter as a plasma plume of 16 cm in diameter. To operate the facility, Argon is employed as starting gas because of the longer lifetime of the free electrons at low pressure compared to air plasma, facilitating the initial electric discharge. Then, the gas is gradually switched to the desired test gas (air, N_2, CO_2) and the argon is switched off.

An absolute pressure transducer (Memberanovac DM 12, Leybold Vacuum) measures the static pressure (p_s) in the test chamber. As the plasma jet is low subsonic (Ma $\approx$ 0.1), the static pressure is assumed constant inside the chamber. The static pressure uncertainty can be considered to be ±10% due to the stability of the vacuum pumps.[28] The gas mass flow rate ($\dot{m}_{gas}$) supplied to the torch is monitored through a calibrated gas rotameter (Bronkhorst EL-Flow F-203AV), while the Plasmatron control system records the electric power (P_{el}) supplied to the induction coil. Suitable quartz windows installed on the two sides of the vacuum chamber provide the necessary optical access in the direction perpendicular to the plasma flow.

DOI: 10.13009/EUCASS2023-591

3.2 Optical emission spectroscopy

The optical system consists of a 750 mm focal length Acton Series SP-2750 Czerny-Turner spectrograph, a 150 mm focal length spherical mirror and a planar mirror. The spectrograph is equipped with a triple grating turret with 150, 1200, and 3600 grooves/mm respectively. The central wavelength of the dispersion can be changed by a software-controlled rotation mechanism, allowing high-resolution spectral scans in a wide range. In the context of this work, the 1200 grooves/mm grating is used for the H_β line, and the 150 grooves/mm grating is used to measure the complete spectrum between 280 and 940 nm. An intensified CCD detector (Princeton Instruments PI-MAX3) with a resolution of 1024×1024 pixels and a pixel size of 12.8 μm is connected to the exit slit of the spectrograph. The spatial magnification factor across the jet diameter is 0.2 mm/pixel. The integration time and intensifier gain are interactively adjusted during the test to reach a high Signal to Noise Ratio (SNR) for each spectral range and test condition.

The calibration of the system in the measurement wavelength range is performed before the testing campaign. The intensity is calibrated with a tungsten ribbon lamp (OSRAM WI 17G) with a known spectral radiance, placed inside the chamber on the jet axis. The methodology follows the procedure presented by Fagnani et al.,[28] and it preserves the optical path as in the actual measurements.

3.2.1 Local emission rebuilding

The radiance emitted at the surface of plasma is resolved in spectral and radial dimensions. As the plasma is observed in the side direction, the recorded spectral radiance results are integrated along the line of sight over the entire depth of the source. Assuming axisymmetry and an optically thin medium, the inverse Abel transformation allows to rebuild the measured spatial distribution of the line of sight integrated signal. To cut high frequency components, the measured signal intensity is smoothed by a low-pass filter in the radial dimension. Then the Abel inversion algorithm is applied. The relation between the spectral radiance L_λ [W m^{-2} sr^{-1} nm^{-1}] and the local spectral emission intensity ε_λ [W m^{-3} sr^{-1} nm^{-1}] as a function of the radial coordinate r from the plasma jet axis is given as

$$\varepsilon_\lambda(r) = -\frac{1}{\pi}\int_r^R \frac{dL_\lambda(y)}{dy}\frac{dy}{\sqrt{y^2 - r^2}} \tag{13}$$

with R being the maximum radial dimension of the plasma jet, where the recorded signal approaches zero.

3.2.2 Plasma Local Thermodynamic Equilibrium temperatures

The local emission intensity of an atomic spectral line occurs when a bound electron undergoes a transition from an upper level (u) of energy E_u to a lower level (l) and is given by[29]

$$\varepsilon_{ul} = \frac{E_u - E_l}{4\pi}\mathcal{A}_{ul} n_{u,i}, \tag{14}$$

where $\mathcal{A}_{ul}$ is the Einstein coefficient of spontaneous emission for the specific transition u $\rightarrow$ l and $n_{u,i}$ is the population density of the exited states of the atomic species i. Assuming Local Thermodynamic Equilibrium (LTE) conditions and Boltzmann distribution, $n_{u,i}$ can be related to the gas temperature (T_{LTE}) as

$$n_{u,i} = n_i\left(T_{LTE}, p\right)\frac{g_{u,i}\exp\left(-\frac{E_{u,i}}{k_B T_{LTE}}\right)}{Q_{int,i}\left(T_{LTE}\right)} \tag{15}$$

where n_i is the number density of species i in the mixture, $g_{u,i}$ is the degeneracy of the energy level $E_{u,i}$, k_B is the Boltzmann's constant, and $Q_{int,i}$ is the internal partition function of the atomic species i. The Einstein's coefficients, degeneracies and energy levels for the considered atomic transitions are obtained using the NIST database,[30] while the partition function is computed from Chauveau et al.[31] Under the assumption of LTE, once the pressure p is fixed, n_i depends only on temperature. Thus, a comparison between the analytically computed emission intensity with the experimentally measured one yields the local plasma LTE temperature.[28]

3.2.3 Broadening mechanisms of the H_β line

The lineshape of the Balmer β transition (4-2) of atomic hydrogen at 486.1 nm is determined by Stark, van der Waals, resonance, natural, Doppler, and instrumental broadening mechanisms. The Stark half-width at half-maximum (HWHM), corresponds to a fit of the widths listed by Gigosos and Cardeñoso[13] for electron densities n_e between 10^{20} m^{-3} and 4×10^{23} m^{-3}. This fit is within ±5% of the values of Gigosos and Cardeñoso for temperatures up to

DOI: 10.13009/EUCASS2023-591

10000 K. The other HWHM expressions of the H_β line are derived by Laux.[7] The expressions for the HWHM [nm] for each of the broadening mechanisms are summarized in Table 1, where n_e is the electron number density [m^{-3}], x_H is the mole fraction of hydrogen atoms, p is the pressure [Pa], and T is the temperature [K].

Table 1: HWHM expressions for each of the broadening mechanisms of the H_β line.

Broadening mechanism	HWHM [nm]
Stark	$4.91 \times 10^{-16} n_e^{0.668}$
Resonance	$2.98 x_H p/T$
Van der Waals	$0.178 p/T^{0.7}$
Natural	3.1×10^{-5}
Doppler	$1.74 \times 10^{-4} T^{0.5}$
Instrumental	0.02442

The convolution of the Stark, resonance, Van der Waals, and natural broadening mechanisms results into a Lorentzian HWHM, that is the sum of the widths of each individual component. On the other hand, the Gaussian profile equals the Doppler broadening. In this work, the instrumental broadening corresponds to a square root of a Voigt profile. Overall, the convolution of the Gaussian shape with the Lorentzian shape results into a Voigt profile and its convolution with the instrumental line space allows to fit the measured H_β line, and consequently to estimate the electron number density in the flow.

3.3 Communication setup

Luís et al.[18] performed a numerical analysis to design a communication system for testing at the Plasmatron, selecting the Ka-band as the most appropriate for signal propagation and blackout testing. Then, they performed an experimental campaign with conical horn antennas (23° beamwidth) at the Plasmatron, and they stated clear ripples due to interferences caused by the windows and the chamber walls. To minimize the effect of the windows, Luís et al. conducted differential measurements. To minimize the reflections on the chamber walls, a new communication system in the Ka-band is proposed. This new system is required to follow three main constraints: an antenna beamwidth smaller than 5°, a maximum aperture of 18 cm (determined by the window size), and circular polarization. The first two constraints (illustrated in Fig. 2a) allow to have the signal propagation concentrated inside of the opposite window (which has a height of 18 cm) at a distance of 2 m. The final setup consists of two sets each comprising a horn lens antenna of 4.2° beamwidth (MI-wave 258A-6/0.250/381) and a waveguide orthomode transducer (MI-wave 281A-35.75/0.250/381/599), sequentially connected in each port to a waveguide to coax adapter (MI-wave 411A/599/KF), to a flexible microwave cable (Huber-Suhner SUCOFLEX 102) and to a DC block (MI-wave 8141A). Further operating details are summarized in Table 2. The transmission and reception of the signal are measured with a 4-ports vector network analyser (Rohde and Schwarz ZNB40). The antennas are aligned perpendicular to the torch exit and placed outside of the chamber next to the side windows (see Fig. 2a).

Table 2: Details about the instruments.

Instrument	Connector	Operating frequency [GHz]	Link budget
Antenna	UG-599	33 - 38.5	32 dBi
Orthomode transducer	UG-599	33 - 38.5	- 0.5 dB
Adaptor	UG-599 - 2.92 mm (f)	26.5 - 40	- 0.4 dB
Cables	2.92 mm (m - f)	up to 46	- 2.62 dB/m
DC block	2.92 mm (m - f)	0.01 - 40	- 0.75 dB
VNA	2.92 mm (m)	0.01 - 40	10 dBm

Alignment and calibration of the test setup are carried out every day of testing. The alignment is done using a 360° self-leveling laser (Makita SK700D), ensuring that the centers of both antennas remain on the horizontal plane passing through the center of the torch, and on the vertical plane at a certain distance from the torch exit. The systematic calibration of the system is performed using a 2.92 mm automatic calibration unit (Rohde and Schwarz ZN-Z54). This type of calibration ensures that the effects of cables and DC blocks, and all systematic errors in general are canceled out before the measurements of the radio signal of the antennas. UOSM (unknown thru-open-short-match) full 2-port calibrations are performed. A combination of three full 2-port calibration ensures that all sixteen S-parameters are fully corrected.[32]

DOI: 10.13009/EUCASS2023-591

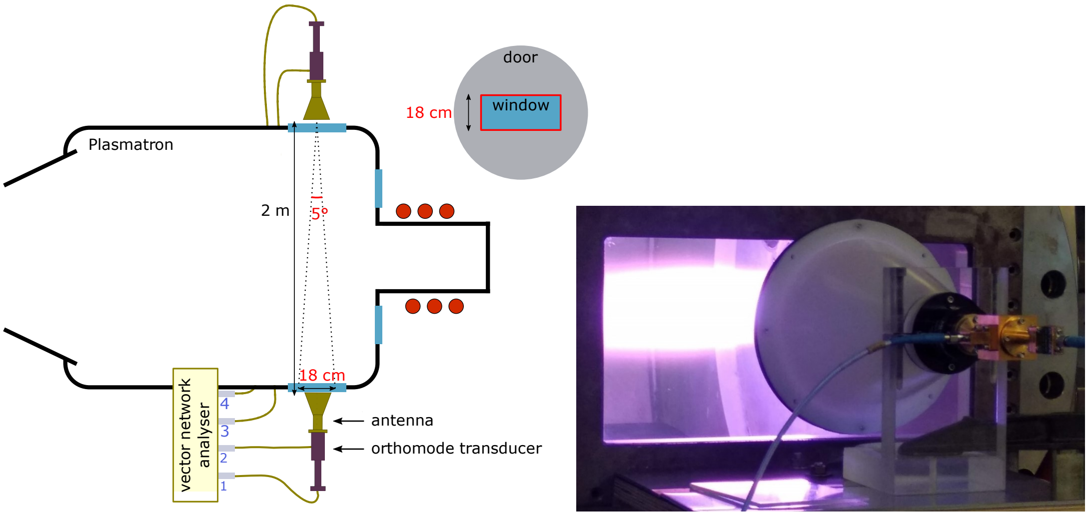

(a) Schematic of the setup and system constraints.

(b) Picture taken during a test.

Figure 2: Experimental setup.

3.3.1 Total attenuation

The measured parameters correspond to the S-parameters described in Section 2.2, that are complex numbers and that can be written, in linear units, as

$$S = |S_{[l.u.]}|e^{i\phi_S}. \tag{16}$$

Experimentally both magnitude $|S|$ [dB] and angle ϕ_S [degrees] are acquired as a function of frequency. In linear units the S parameters are proportional to the electric field $|E|$ and are computed as $|E| \propto 10^{|S_{[dB]}|/20}$.

The orthomode transducer separates and combines (at the transmitting and receiving antennas, respectively) the two orthogonally linearly polarized signals caused by the circular polarization nature of the antennas. In this case, each component (vertical and horizontal) of the transmitting signal is sent individually and both components of the receiving electric field are actually measured. This means that, besides minimizing the reflections on the walls, this setup allows to untangle the attenuation and Faraday rotation of the signal that occur simultaneously when propagating through an ionized medium. The computation of the resulting electric field is performed considering both of the components as

$$|E| = \sqrt{|E_V|^2 + |E_H|^2}, \tag{17}$$

being V and H the vertical and horizontal components, respectively, ultimately neglecting the rotation of the electric field. Considering the notation attributing ports 1 and 2 to the vertical and horizontal components of the transmitting antenna $(1, V$ and $2, H)$ and ports 3 and 4 the vertical and horizontal components of the receiving antenna $(3, V$ and $4, H)$, the total losses L correspond exactly to the resulting electric field, and in linear units reads as

$$L_i = \sqrt{|E_{3i}|^2 + |E_{4i}|^2}, \quad i \in \{1, 2\}. \tag{18}$$

To study the influence of the plasma, the attenuation between the averaged total losses with and without plasma is considered in this study. This method allows to neglect the influence of the quartz windows and any intrinsic reflections on the metallic walls of the chamber. In linear units, the mean attenuation can be written based on the averaged total losses as

$$\overline{A} = \frac{\overline{|L_{ON}|}}{\overline{|L_{OFF}|}} \tag{19}$$

or, equivalently, in decibels [dB] as

$$\overline{A}_{[dB]} = 20\log_{10}(\overline{A}_{[l.u.]}) = \overline{L_{ON}}_{[dB]} - \overline{L_{OFF}}_{[dB]}. \tag{20}$$

The main source of uncertainty considered in this work is the random standard uncertainty ($\sigma_{\overline{|L|}}$), which depends on the number of samples N acquired during a certain condition. This uncertainty can be defined, for a normally distributed population and large number of samples, as

$$\sigma_{\overline{|L|}} = \frac{\sigma_{|L|}}{\sqrt{N}} \times 1.96, \tag{21}$$

DOI: 10.13009/EUCASS2023-591

for a 95% confidence interval. The standard deviation of the mean attenuation due to the plasma is computed according to Taylor's expansion, and ultimately it can be written as

$$\sigma_{\overline{A}} = \sqrt{\left(\frac{1}{|\overline{L_{OFF}}|}\right)^2 \sigma^2_{|\overline{L_{ON}}|} + \left(-\frac{|\overline{L_{ON}}|}{|\overline{L_{OFF}}|^2}\right)^2 \sigma^2_{|\overline{L_{OFF}}|}}. \tag{22}$$

being $\sigma_{|\overline{L_{OFF}}|}$ and $\sigma_{|\overline{L_{ON}}|}$ the standard deviations of the mean total losses in vacuum and in a plasma flow, respectively. To plot the mean attenuation with error bars in decibels [dB], the following method is implemented

$$20\log_{10}\left(\overline{A} \pm \sigma_{\overline{A}}\right), \tag{23}$$

either as function of frequency or as a total averaged values over the frequency range.

3.3.2 Faraday rotation

Following the same notation, the vertical and horizontal components of the signal received by, respectively, ports 3 and 4 ($3, V$ and $4, H$) can be written as function of the transmitting components as

$$\begin{bmatrix} E_{4,H} \\ E_{3,V} \end{bmatrix} = \begin{bmatrix} \cos\theta_F & -\sin\theta_F \\ \sin\theta_F & \cos\theta_F \end{bmatrix} \begin{bmatrix} E_{2,H} \\ E_{1,V} \end{bmatrix}. \tag{24}$$

If rotation does not occur ($\theta_F = 0$), then the received vertical/horizontal component is equal to the transmitted vertical/horizontal component respectively, and zero at the orthogonal projection. Untangling the attenuation, the Faraday rotation can be estimated with any of the transmitting parameters as

$$\begin{cases} \cos\theta_F = |E_{31}|/L_1 \\ \sin\theta_F = |E_{41}|/L_1 \end{cases}, \qquad \begin{cases} \cos\theta_F = |E_{42}|/L_2 \\ \sin\theta_F = -|E_{32}|/L_2 \end{cases}. \tag{25}$$

The theoretical Faraday rotation can be estimated from the expression given in Eq. 9, that depends on the strength of the magnetic field, the wave frequency and the TEC. The magnetic field of the Plasmatron coil can be estimated as the sum of the magnetic field for individual circular loops.[33] Simple analytical expressions for the magnetic field for a circular loop currying a static current are derived by Simpson et al.[34] For a current loop carrying a current I, with radius a, located in the $x - y$ plane and centered at the origin, the magnetic field components in Cartesian coordinates are given by

$$\begin{aligned} B_x &= \frac{Cxz}{2\alpha^2\beta\rho^2}\left[\left(a^2 + r^2\right)E\left(k^2\right) - \alpha^2 K\left(k^2\right)\right] \\ B_y &= \frac{y}{x}B_x \\ B_z &= \frac{C}{2\alpha^2\beta}\left[\left(a^2 - r^2\right)E\left(k^2\right) + \alpha^2 K\left(k^2\right)\right] \end{aligned} \tag{26}$$

being $\rho^2 = x^2 + y^2$, $r^2 = x^2 + y^2 + z^2$, $\alpha^2 = a^2 + r^2 - 2a\rho$, $\beta^2 = a^2 + r^2 + 2a\rho$, and $C = \mu_0 I/\pi$. μ_0 is the permeability of vacuum, and $E\left(k^2\right)$ and $K\left(k^2\right)$ are the elliptic integrals in spherical coordinates (r, θ, ϕ) with argument

$$k^2 = \frac{4ar\sin\theta}{a^2 + r^2 + 2ar\sin\theta}. \tag{27}$$

3.4 Testing conditions

For studying the signal propagation and to correlate it with the electron number densities, several conditions covering the operational envelope of the Plasmatron are tested. The test gas is air and the testing conditions are summarized in Table 3. Emission spectroscopy is only conducted for the conditions marked with a star.

For each of the targeted pressures, the radio signal is measured for twenty samples without plasma. To proceed with the experiments, the Plasmatron is switched on and the air mass flow is set to 16 g/s with the calibrated rotameter. The vacuum pumps are regulated until the target static pressure is reached inside the chamber. Once the required conditions are reached, fifty radio signal consecutive samples are taken. For each condition tested, an average and standard deviation are computed in linear units.

For the spectroscopy measurements, five images are taken for each of the wavelengths interval with plasma, using a mixture of air and 2% mole fraction of H_2. A baseline spectrum around 486 nm is also measured using synthetic air, and a background image is obtained without plasma for the same grating, gain and gate time conditions as measured with plasma.

DOI: 10.13009/EUCASS2023-591

Table 3: Summary of testing conditions.

Distance [mm]	Static pressure [mbar]	Electric power [kW]
300	15	100, 125, 150, 175, 200, 250, 300, 320, 350, 400, 450, 500, 550, 600
300	50	100, 125, 150, 175, 200*, 250, 300, 320*, 350, 400*, 450, 500*, 550, 600*
300	100	125, 150, 175, 200*, 250, 300, 320*, 350, 400*, 450, 500*, 550, 600*

4. Experimental results

4.1 Temperature and electron number density

Figure 3 shows the radial distribution of the temperature, and electron number density and corresponding plasma frequency, for different pressure and power settings at 300 mm from the torch exit. The temperature uncertainty is 10% and the error bars are omitted for simplicity. To note that the temperature and consequently the electron number density, and the numerical estimations done with Mutation++ library[35] assume that the flow is in LTE. Figure 3a presents the temperature extracted from the O line at 777 nm, for pressures of 50 and 100 mbar (orange and green lines, respectively). The horizontal dashed lines correspond to the numerical temperature computed with Mutation++ library at which, for each pressure, the electron number density is higher than 5×10^{19} m^{-3}, which corresponds to the threshold to which the fitting for the Stark broadening is valid. Observing the evolution of the temperature distribution, it is clear that for 200 kW, the electron densities are too low to be measured experimentally with the followed approach. Thus, Fig. 3b presents only the radial distribution of the experimentally measured electron number density for a power of 400 kW. The banded regions correspond to the estimation of the electron number densities computed with Mutation++ (M++) based on the measured temperature and considering its 10% uncertainty. The experimental and theoretical measurements of the electron densities for 400 kW considering the uncertainties match well up to around half of the profile, from which the intensity of the spectral lines gets too low for good fitting. The numerical estimation of the electron number densities for the temperatures measured at 200 kW are below the threshold of 5×10^{19} m^{-3} (dashed grey line), but at the core of the jet still above the radio signal frequency of the antennas (horizontal red shaded band). Further analysis between the electron number density and the radio signal propagation is conducted in the next section.

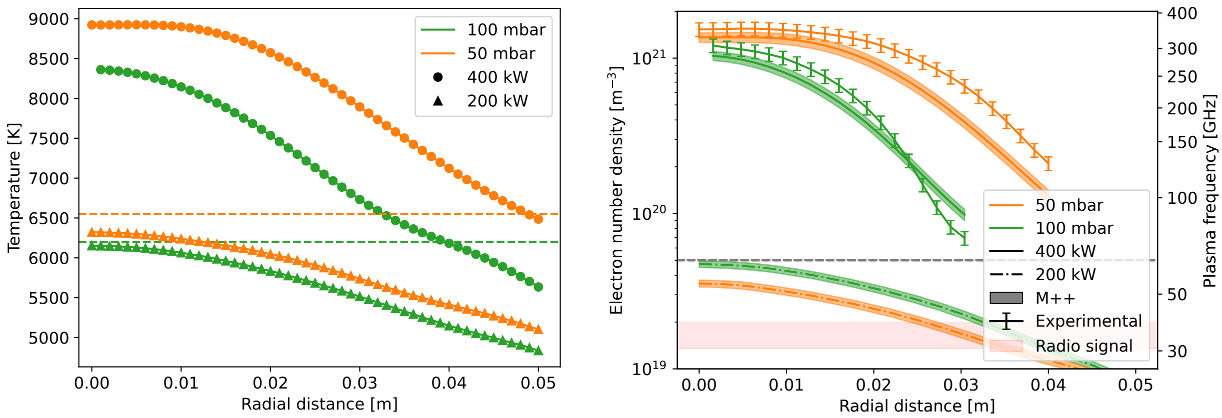

(a) Experimental temperature.

(b) Electron number density and corresponding plasma frequency.

Figure 3: Radial profiles for different pressures and power settings.

4.2 Signal propagation

4.2.1 Estimation of wall reflections

From the gains and losses in the communication system (Table 2), a theoretical transmitted magnitude can be estimated to compare with experimental measurements without plasma. The radio link budget sums the transmitted power along with the gains and losses of every subsystem to determine the signal strength arriving at the receiver input.

DOI: 10.13009/EUCASS2023-591

For this case, the link budget equation for the radio communication system is written as

$$P_R - P_T = G_T - L_T - L_{FS} + G_R - L_R, \tag{28}$$

where $P_R - P_T$ [dB] is the ratio (in linear units) of the received and transmitted powers (converted to dB) as measured by the VNA. G_T and G_R are, respectively, the transmitter and receiver antenna gains [dBi], L_T and L_R are the losses [dB] associated to transmitter and receiver adaptors, mismatching on the line (0.07 dB for given VSWR of 1.3) and caused by the windows, and L_{FS} the free space loss [dB]. The losses due to the windows are considered to be the same as presented by Luís et al.,[18] since the testing frequencies and windows are the same in both works. As the calibration is done between the cable and the adaptor, the losses associated with the cables and DC blocks are considered in the measurements, and therefore do not need to be accounted for in the link budget. The free space losses can be estimated as

$$L_{FS} = 20\log_{10}\left(\frac{4\pi d f}{c}\right) \tag{29}$$

where d is the distance between the antennas, f the operating frequency, and c the speed of light. For this experimental campaign the antennas are positioned 2 m from each other.

Figure 4 presents the magnitude of the S_{31} (blue line) and S_{32} (orange line) coefficients overlapped with the theoretical link budget (grey line) as function of frequency. To remember that ports 1 and 3 correspond to vertical components of the wave, while port 2 (and 4) corresponds to the horizontal component. The theoretical estimation and experimental results for S_{31} are matching very well with a mean difference of 0.8 dB. The same exercise for the data presented by Luís et al.[18] yields a mean difference of 1.8 dB. This shows a clear improvement of the setup, as there is a clear reduction of the reflections on the walls. Regarding the S_{32} coefficient, the values measured correspond to the cross-polar limit which define the minimum measurement threshold. Additionally, the lowest the magnitude of the signal, the higher the associated uncertainty, and thus the higher the measured ripples.

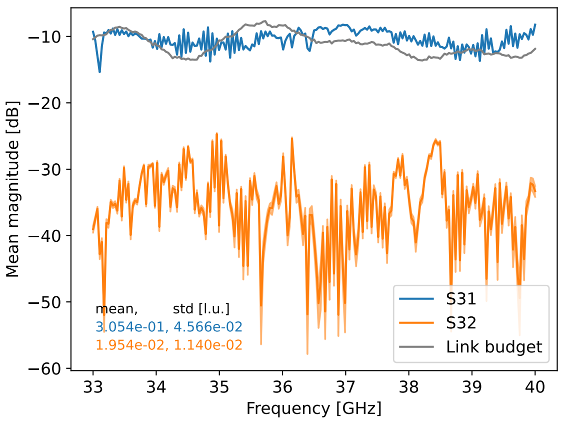

Figure 4: Magnitude of the S_{31} and S_{32} parameters overlapped with the theoretical link budget.

4.2.2 Signal attenuation due to the plasma

As example, Fig. 5 presents 6 S-parameters out of the 16 measured in function of frequency in vacuum (blue lines) and with plasma (orange lines) for a test case at 100 mbar, 400 kW, 300 mm from the torch exit. Total averaged quantities and standard deviations are also shown. Parameters S_{12}, S_{21}, S_{34} and S_{43} correspond to coefficients between ports on the same antenna, so they do not have a physical meaning. The reflection coefficients as a function of the frequency are almost constant in both cases with and without plasma. The same behaviour is observed for the other two S_{ii} parameters. The transmission coefficients (S_{ij}, $i \neq j$) show a clear attenuation of the signal when propagating through the plasma. For the signal propagating through the components with the same orientation ($V - V$ or $H - H$), there is an average signal decay of 30 dB, while for the components aligned perpendicularly ($V - H$ or $H - V$) the average decay is of 16 dB. The decay on the latest proves that there is Faraday rotation (because there is a change of the signal intensity), but also attenuation. The same behaviour is observed for the transmission coefficients not presented, as the S matrix is symmetric and thus $S_{ij} = S_{ji}$.

To estimate the total losses of the signal, neglecting its rotation, the resulting electric field relating each component of the receiving antenna with one of the components of the transmitting antenna (e.g. $V - V$ and $H - V$) is

DOI: 10.13009/EUCASS2023-591

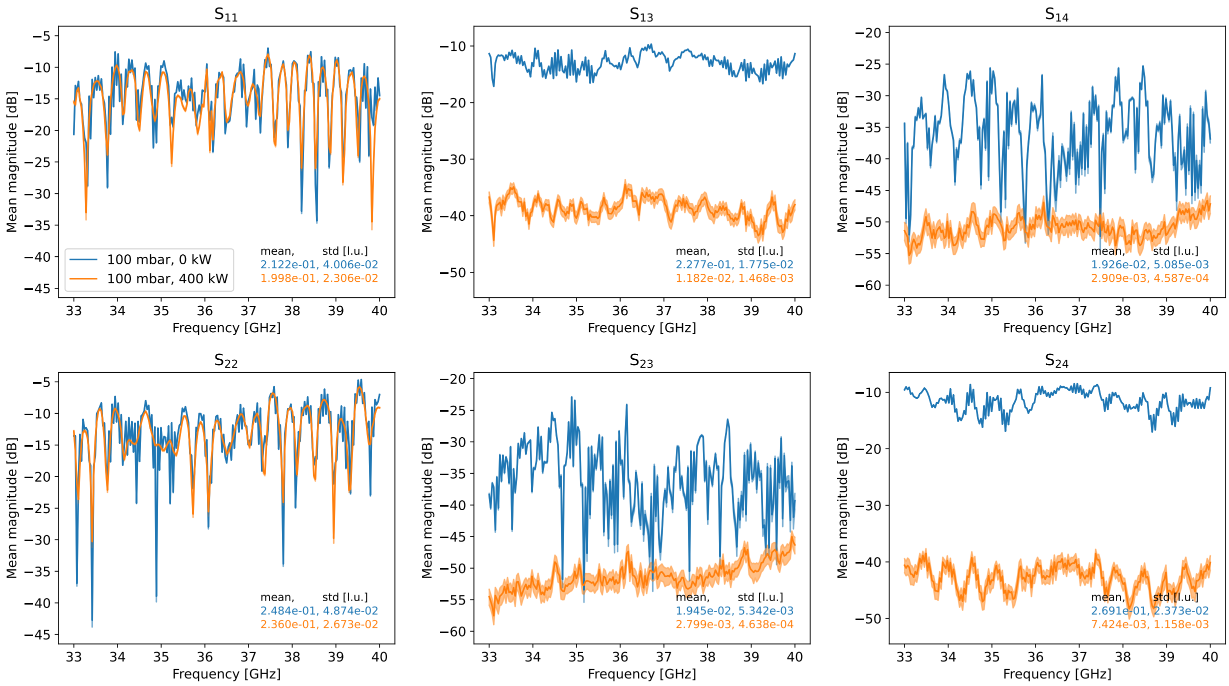

Figure 5: Variation of the mean magnitude of the S parameters for 100 mbar, 400 kW.

computed according to Eq. 18. Figure 6 presents the total losses for the signal sent by the vertical components of antenna 1, for the case without plasma (blue line) and with plasma (orange line). For the case without the plasma, the total attenuation is almost equal to the S_{13} parameter since there is no rotation of the signal, thus the signal is mainly propagating through the co-polar direction, as expected. For the case with plasma there is a slight contribution of the cross-polar component and a mean total loss of 38 dB. Overall, for this case, the total attenuation due to the plasma is in average 25 dB (grey line in Fig. 6). The same behaviour is observed for the L_2, L_3 and L_4 total attenuation coefficients.

According to the measured electron number densities (Fig. 3b), the maximum plasma frequency for this testing condition is 312 GHz, which is almost 8 times higher than the radio frequency signal transmitted. Figure 7 represents the variation of plasma, gyroscopic and collisional frequencies, and the interval of the sweeping radio signal. The gyroscopic frequency is computed based on the magnetic field estimated in the next section and represented in Fig. 9. This frequency is eight orders of magnitude lower than the plasma frequency, and its effect can be neglected, thus considering a non-magnetized medium. Even though the collisional frequency is also much lower than the plasma frequency (but less than two orders of magnitude), the ratio between the collisional and signal frequency equals to around 0.3 at the axis of the jet. This ν/f ratio is represented in Fig. 1a, with a zoom in a region up to f_p/f equal to 8. Even for this amount of collisions, μ is never zero and total reflection does not occurs. The signal is however attenuated due to collisions, as observed experimentally.

4.2.3 Quantification of the Faraday rotation

Figure 8 presents the mean Faraday rotation obtained experimentally from the S_{31} parameter with respective standard deviation, overlapped with a numerical estimation of the Faraday rotation. The experimental Faraday rotation is obtained by subtracting any inherent rotation of the antennas (measurements without plasma) from the rotation calculated with the plasma. The Faraday rotation computed from S_{41} and S_{42} equals exactly, respectively, S_{31} and S_{32}. Small differences between the values of the Faraday rotation for S_{31} and S_{32} are related with the unsteadiness of the plasma (as quantified and explained by Luís et al.[18]) that occurs during the measurement of the different parameters.

The numerical estimation of the Faraday rotation is computed from Eq. 9, and it depends on the magnetic field strength, the total electron content (TEC) and the frequency of the antennas. The TEC is computed from the measured electron number density profile (Fig. 3b). The magnetic field is estimated numerically based on the equations for a single loop (Eq. 26) centered at 127 mm and by summing it with the same magnetic field shifted to 177, 227, 277, 327 and 377 mm (position of the coils). The radius of the coil is 109 mm, and the current it carries is acquired by the Plasmatron data acquisition system. The magnetic field of the Earth in the lab is also considered ($B_x = -22.6\mu$T,

DOI: 10.13009/EUCASS2023-591

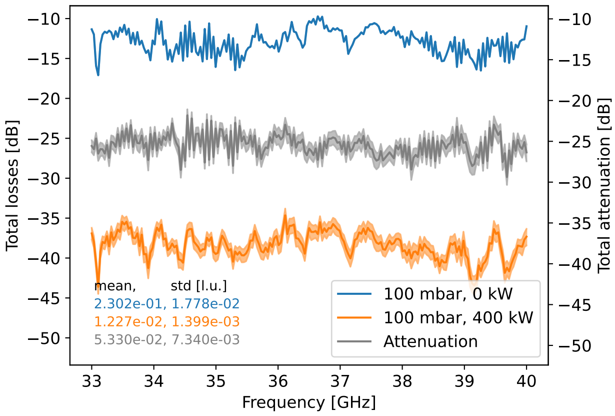

Figure 6: Variation of total losses L_1 and total attenuation for 100 mbar, 400 kW.

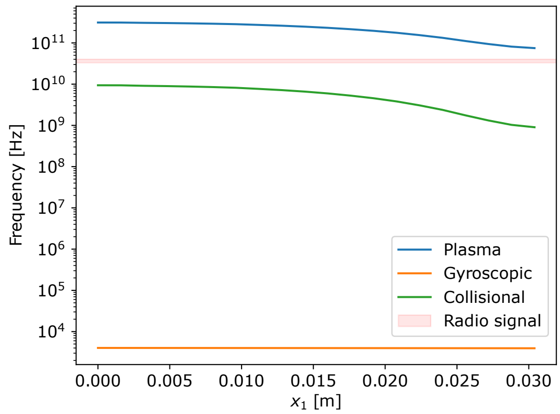

Figure 7: Variation of the plasma, gyroscopic and collisional frequencies for 100 mbar, 400 kW.

$B_y = -45.8\mu$T and $B_z = 11.7\mu$T) and each components in summed to the analytical magnetic field of the coils. For the exemplifying test case, the current on the coil is 327.1 A and the distribution of the resulting magnetic field strength, for $y = 0$ m (symmetry axis) is represented in Fig. 9. The same Fig. is overlapped with the total magnetic field strength at $z = 0$ m as a function of x (blue line), and at $z = 0.783$ m (which corresponds to 300 mm from the torch exit) as a function of z (red line).

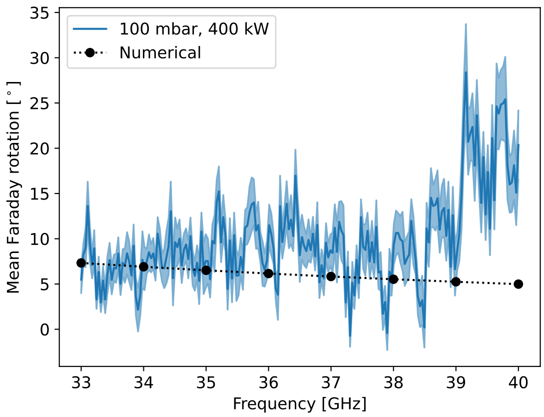

Figure 8: Variation of the Faraday rotation for 100 mbar, 400 kW.

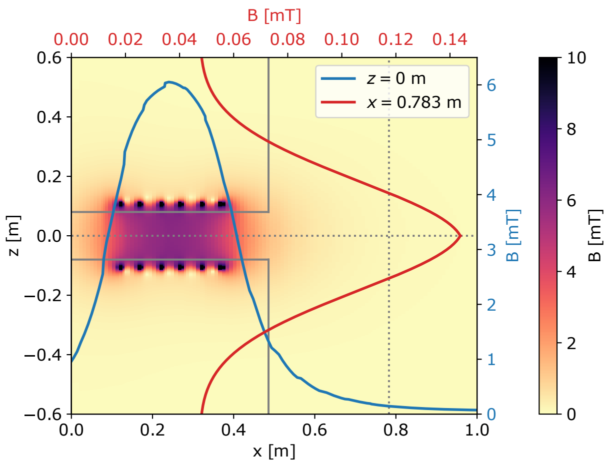

Figure 9: Distribution of the magnetic field in the chamber for 100 mbar, 400 kW (327.1 A).

Overall the experimental and numerical results show a good agreement, except for higher radio signal frequencies. This is also observed for the other conditions. According to the theoretical Eq. 9, the Faraday rotation is inversely proportional to the square of the frequency of the signal. As such, for higher frequencies the rotation should be lower (as observed by the theoretical estimation). However, the theoretical expression assumes that the signal only propagates in a straight line ds, when in reality, the antenna has a radiation pattern and emits over a volume in space, which is not constant due to the jet profile. Additionally, the radiation pattern is also dependent on the frequency. As the beamwidth of the antenna decreases with frequency, for higher frequencies the signal propagates more in the core of the jet, which corresponds to a zone of higher electron densities. Hence, the numerical estimation of the TEC is underestimated for higher signal frequencies, due to the considered propagation path.

4.2.4 Parametric study

Data analysis considering the dynamic nature of the plasma jet makes drawing conclusions about radio signal propagation challenging. Therefore, it is of interest to neglect the jet fluctuations, assume a steady state flow as normally done for thermal analysis in this type of facility, and consider total averaged quantities throughout the frequency range of each measurement. Figure 10 represents the variation of the total attenuation (Eq. 19) as a function of frequency

DOI: 10.13009/EUCASS2023-591

and power for 100 mbar. As the attenuation is almost constant as a function of frequency (as seen also in Fig. 6) for each of the testing conditions, its values are averaged through the entire sweeping frequency range. The same methodology has been been followed by Luís et al.[18] Thus, the total attenuation is plotted as a function of power for different chamber pressures and power settings in Fig. 11. Standard deviations are also shown here as error bars around the mean value. Clear attenuations are observed when increasing power and, consequently, electron number densities. With this configuration, the mean total attenuation varies between -12 and -37 dB when increasing electric power. Luís et al.[18] have stated total magnitude differences between -5 and -14 dB for the same testing conditions. In their work, the antennas had linear polarization and a much larger beamwidth. The first characteristic of their antennas should actually yield a higher attenuation (more negative) than supposed because the Faraday rotation is neglected. Thus, some of the signal is not actually attenuated, but has suffered a rotation of its polarization, being just a component of the transmitted signal measured. The latter characteristic is considered to be the main reason for the discrepancies between the results. Since their antennas have higher beamwidth, a higher portion of the signal is transmitted around the jet that consequently reaches the effective measurement area of the receiving antenna undistributed. Additionally, this also increases the reflections on the walls, increasing the signal magnitude read by the receiving antenna. Furthermore, Luís et al. have stated that no significant changes were observed when increasing pressure. In this work, the choice of a reduced beamwidth for the antennas has also improved the sensitivity of the results with respect to pressure.

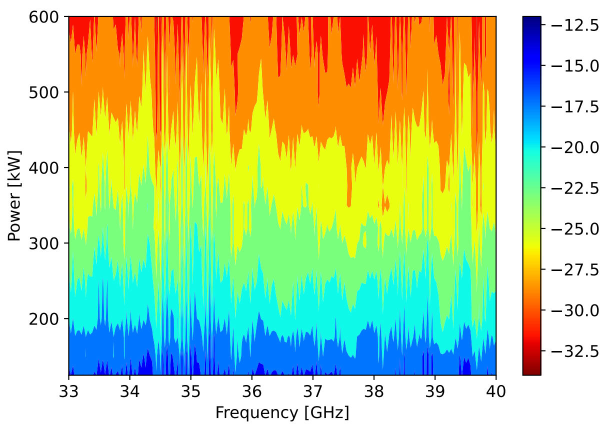

Figure 10: Variation of the total attenuation as a function of frequency and power for 100 mbar.

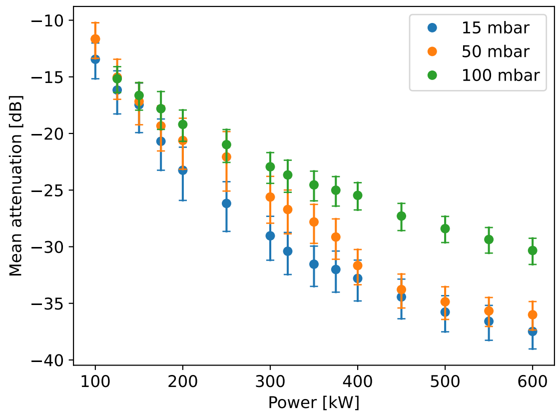

Figure 11: Variation of the mean total attenuation as a function of pressure and power.

The attenuation increases with decreasing pressures, reaching differences of up to 10 dB for the same power. At 50 mbar the jet core is hotter (see Fig. 3a) and narrower than at 100 mbar. At high powers, this translates in higher number of electron densities and higher attenuation (as seen in Fig. 11). Additionally, the narrower core of the jet implies higher collisions so even higher attenuation at lower pressures. At lower powers, the dependence with pressure is not as evident: on one hand, the electron number densities are higher for higher pressures, but on the other hand the number of collisions is lower. For 15 mbar, the flow is expected to be in non-equilibrium, and thus the electron number densities are higher and consequently the attenuation as well. This assumption is recommended to be verified as future work.

Figure 12 shows the variation of of the experimentally obtained Faraday rotation as a function of frequency and power for 100 mbar. As seen in Fig. 8, an increase of rotation is always verified for higher frequencies. As explained in Section 4.2.3 the beamwidth of the antennas decreases with frequency, hence for higher frequencies the signal propagates more in the core of the jet, where there is a higher concentration of the electrons. When increasing power there is also an increase of the rotation because there are more electrons on the flow as well as higher attenuation (as seen in Fig. 10). For the other tested pressures, the same trends are observed with higher angles of rotation: while for 100 mbar, the rotation varies between 0° and 39°, for 50 mbar it varies between 0° and 47°, and for 15 mar between 0° and 49°.

5. Conclusion

Radio signal propagation in an air plasma flow has been studied for a combination of static pressures and power settings. The tests have been conducted by placing two highly directive antennas across the plasma jet at the VKI-Plasmatron facility, and by measuring their signals with a vector network analyser. The proposed experimental setup has allowed to conduct measurements of attenuation and Faraday rotation (rotation of of the electric field vector) due to the plasma. Additionally, using emission optical spectroscopy, the radial distribution of the jet temperature and electron number density have been estimated.

DOI: 10.13009/EUCASS2023-591

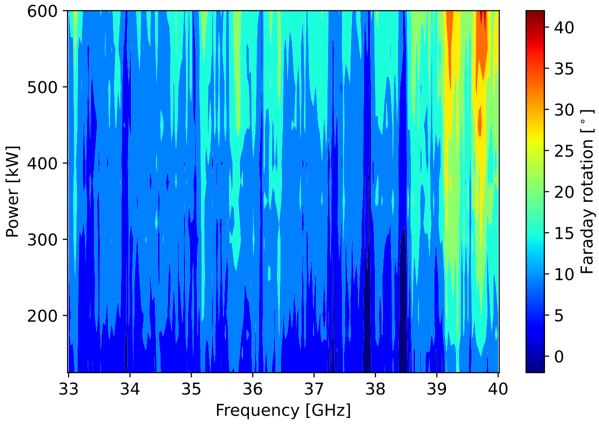

Figure 12: Variation of the Faraday rotation as a function of frequency and power for 100 mbar.

The measured electron number density profiles based on the Strak broadening of the H_β line have shown a good agreement with the numerical estimations using Mutation++ library with the measured temperature profiles. For lower powers, the electron number densities are below the threshold to which the fitting is valid, and thus, they could not be inferred experimentally. Additionally, the estimation of the jet temperature assumes LTE conditions, which may not be the case at 15 mbar. Other non-intrusive measurement techniques, as interferometry or reflectometry, are advised as future work to be able to measure the electron number densities at lower powers and low pressures, and to access the non-equilibrium assumption.

The radio signal propagation has been studied initially without plasma to quantify the reflections on the chamber walls. A very good agreement has been observed between the experimental measurements and the theoretical link budget, corroborating the hypothesis that almost no reflection occur. Nevertheless, to minimize these effects and the free space losses, the effect of the plasma has been studied based on the difference between the signal with and without plasma. To neglect the influence of the plasma unsteadiness, the signal has been averaged over a large number of samples. Analysing the transmission coefficients, clear attenuations have been verified in both co- and cross-polar components. The Faraday rotation has also been computed from experimental results. A good agreement has been observed when comparing the latter with the numerical estimations. An exception has been verified for higher radio signal frequencies, due to the assumption of straight line propagation path, that neglects the frequency dependent radiation pattern, and the jet thickness.

As no significant changes have been observed over the frequency range and assuming a steady state flow, the attenuation results have been averaged throughout the total frequency range. Their evolution has been analysed in function of pressure and power settings and clear dependencies have been observed. Attenuations of the signal have been verified ranging between -12 and -37 dB depending on the testing conditions, increasing with the increase of power (and consequently electron number densities), and decreasing with pressure. The Faraday rotation has been observed to vary between 0° and 49°, increasing with power and decreasing with pressure. Overall, the signal propagation results comply with the temperature and electron number density results obtained experimentally.

6. Acknowledgements

Diana Luís research is funded by a doctoral fellowship (2021.04930.BD) granted by Fundação para a Ciência e Tecnologia (FCT Portugal). The research of Andrea Fagnani is supported by a doctoral fellowship awarded from the Research Foundation Flanders. The MEESST project is funded by the European Union's Horizon 2020 research and innovation programme under grant agreement No 899298.

References

[1] L. Tonks and I. Langmuir. A General Theory of the Plasma of an Arc. *Phys. Rev.*, 34(6), September 1929. `https://doi.org/10.1103/PhysRev.34.876`.

[2] B. Brichard. Implementation of and Electrostatic Probe as a Plasma Diagnostic Technique. Technical Report 1997-05, von Karman Institute for Fluid Dynamics, June 1997.

DOI: 10.13009/EUCASS2023-591

[3] S. Holum, A. Viladegut, D. Luis, and O. Chazot. Determination of Electron Number Density in ICP Facility. Technical report, von Karman Institute for Fluid Dynamics, June 2022.

[4] J. Sánchez, B. Branas, T. Estrada, E. de la Luna, and V. Zhuravlev. Amplitude modulation reflectometry for large fusion devices. *Review of Scientific Instruments*, 63(4654), 1992. `https://doi.org/10.1063/1.1143651`.

[5] O. Bogar, J. Zajac, F. Zacek, M. Varavin, M. Hron, R. Panek, and A. Silva. Microwave reflectometer for density profile and turbulence measurements on the COMPASS tokamak. *Review of Scientific Instruments*, 91(1), 2020. `https://doi.org/10.1063/1.5099345`.

[6] S. Mota, D. P. Resendes, and L. Cupido. Plasma Reflectometry Applied to Plume Density Measurements of Electric Propulsion Thrusters. In *31st International Electric Propulsion Conference*, September 2009.

[7] C. O. Laux, T. G. Spence, C. H. Kruger, and R. N. Zare. Optical diagnostics of atmospheric pressure air plasmas. *Plasma sources Science and Technology*, 12:125–138, 2003. `https://doi.org/10.1088/0963-0252/12/2/301`.

[8] D. Le Quang Huy. *Spectroscopic measurements of sub- and supersonic plasma flows for the investigation of atmospheric re-entry shock layer radiation*. PhD thesis, Université Blaise Pascal and von Karman Institute for Fluid Dynamics, 2014.

[9] C. R. Vidal, J. Cooper, and E. W. Smith. Hydrogen stark-broadening tables. *The Astrophysical Journal supplement*, 214, 1973. `https://doi.org/10.1086/190264`.

[10] D. E. Kelleher and W. L. Wiese. Observation of ion motion in hydrogen Stark profiles. *Physics Review Letters*, 31(1431), 1973. `https://doi.org/10.1103/PhysRevLett.31.1431`.

[11] W. L. Wiese, D. E. Kelleher, and V. Helbig. Variations in Balmer-line Stark profiles with atom-ion reduced mass. *Physical Review A*, 11(1854), 1975. `https://doi.org/10.1103/PhysRevA.11.1854`.

[12] J. Seidel. Hydrogen Stark Broadening by Model Electronic Microfields. *Zeitschrift fÃ¼r Naturforschung*, 32 a:1195–1206, 1977.

[13] M. A. Gigosos and V. Cardenoso. New plasma diagnosis tables of hydrogen Stark broadening including ions dynamics. *Journal of Physics B: Atomic, Molecular and Optical Physics*, 26(20), 1996.

[14] M. A. Gigosos, M. A. Gonzalez, and V. Cardenoso. Computer simulated Balmer-alpha, -beta and -gamma Stark line profiles for nonequilibrium plasmas diagnostics. *Spectrochimica Acta Part B*, 58:1489–1504, 2003.

[15] D. Le Quang, Y. Babou, and P. Andre. Experimental assessment of local thermodynamic equilibrium in vki plasmatron air plasma jet. *Journal of Technical Physics*, 50(3):151–162, 2009. `https://hal.archives-ouvertes.fr/hal-00578973`.

[16] J. P. Rybak and R. J. Churchill. Progress in Reentry Communications. *IEEE Transactions on Aerospace and Electronic Systems*, AES-7(5):879–894, 1971. `https://doi.org/10.1109/TAES.1971.310328`.

[17] C. Jones. Report from the Workshop on Communications Through Plasma During Hypersonic Flight. *AIAA Meeting Paper*, August 2006. `https://doi.org/10.2514/6.2009-1718`.

[18] D. Luís, A. Viladegut, A. Camps, and O. Chazot. Effect of electron number densities on the radio signal attenuation in an inductively coupled plasma facility. In *9th European Conference for Aeronuatics and Space Sciences (EUCASS)*, June-July 2022. `https://doi.org/10.13009/EUCASS2022-6128`.

[19] A. Lani, V. Sharma, and V. F. Giangaspero *et al.* A magnetohydrodynamic enhanced entry system for space transportation: MEESST. *Journal of Space Safety Engineering*, 10(1), March 2023. `https://doi.org/10.1016/j.jsse.2022.11.004`.

[20] R. Starkey, R. Lewis, and C. Jones. Plasma Telemetry in Hypersonic Flight. In *International Telemetering Conference, International Foundation for Telemetering*, 2002. Paper 02-15-2.

[21] R. Starkey, R. Lewis, and C. Jones. Electromagnetic Wave / Magnetoactive Plasma Sheath Interaction for Hypersonic Vehicle Telemetry Blackout Analysis. In *34th AIAA Plasmadynamics and Lasers Conference*, number AIAA Paper 2003-4167, 2003. `https://doi.org/10.2514/6.2003-4167`.

DOI: 10.13009/EUCASS2023-591

[22] M. Kim. *Electromagnetic manipulation of plasma layer for re-entry blackout mitigation*. PhD thesis, Department of Aerospace Engineering, University of Michigan, 2009.

[23] J. G. Proakis and M. Salehi. *Fundamentals of Communication Systems*. Pearson, 2014. ISBN: 9780133354850.

[24] K. Davies. *Ionospheric radio propagation*, volume 80. US Department of Commerce, National Bureau of Standards, 1965.

[25] F. Caspers. RF engineering basic concepts: S-parameters. *CERN Yellow Report*, CERN-2011-007:67–93, 2011. `https://doi.org/10.48550/arXiv.1201.2346`.

[26] B. Bottin, O. Chazot, M. Carbonaro, V. Van Der Haegen, and S. Paris. The VKI Plasmatron Characteristics and Performance. *Measurement Techniques for High Enthalpy and Plasma Flows*, April 2000.

[27] B. Bottin. *Aerothermodynamic Model of an Inductively-Coupled Plasma Wind Tunnel: Numerical and Experimental Determination of the Facility Performance*. PhD thesis, von Karman Institue for Fluid Dynamics, 1999.

[28] A. Fagnani, D. Le Quang Huy, B. Helber, S. Demange ans A. Turchi, O. Chazot, and A. Hubin. Investigation of a Free-Stream Air Plasma Flow by Optical Emission Spectroscopy and Comparison to Magnetohydrodynamics Simulations. In *AIAA SciTech Forum*, January 2020.

[29] H.-J. Kunze. Introduction to Plasma Spectroscopy. In *Springer Series on Atomic, Optical, and Plasma Physics*. Springer, 2009. `https://doi.org/10.1007/978-3-642-02233-3`.

[30] A. Kramida, Y. Ralchenki, and J. Reader. NIST Atomic Spectra Database, April 2014. `http://physics.nist.gov/PhysRefData/ASD/index.html`.

[31] S. Chauveau, C. Deron, M. Perrin, P. Riviére, and A. Soufiani. Radiative transfer in LTE air plasmas for temperatures up to 15,000 K. *Journal of Quantitative Spectroscopy and Radiative Transfer*, 46(7):113–130, 2003. `https://doi.org/10.1016/S0022-4073(02)00080-8`.

[32] M. Hiebel. Vector Network Analyzer (VNA) Calibration: The Basics. Technical report, Rohde & Schwarz, 2008. `https://pchene.files.wordpress.com/2019/08/8e60b68a24a4169eecbd0763d4a9287037e4.pdf`, last accessed 25 Oct 2022.

[33] J. Lane, R. Youngquist, C. Immer, and J. Simpson. Magnetic Field, Force, and Inductance Computations for an Axially Symmetric Solenoid. Technical Report 2013-217918, NASA, April 2001.

[34] J. Simpson, J. Lane, C. Immer, and R. Youngquist. Simple Analytic Expressions for the Magnetic Field of a Circular Current Loop. 2001.

[35] M. J. B. Scoggins. *Development of numerical methods and study of coupled flow, radiation, and ablation phenomena for atmospheric entry*. PhD thesis, von Karman Institute for Fluid Dynamics and CentraleSupélec, 2017.